Wave Motion 147 (2026) 103812

Contents lists available at ScienceDirect

Wave Motion

journal homepage: www.elsevier.com/locate/wamot

Slow-sound in an acoustic resonator-mounted duct: assessment model and transient experiments

Jinze Li, Xiang Yu, Li Cheng *

Department of Mechanical Engineering, The Hong Kong Polytechnic University, Kowloon, Hong Kong, China

ARTICLE INFO

Keywords:
Slow-sound effect
Acoustic resonator
Effective medium approach
Transient analysis

ABSTRACT

Acoustic designs based on wave velocity manipulation offer new possibilities for realizing high performance acoustic devices. Sophisticated acoustic systems are mostly constructed through embedding basic acoustic components such as quarter-wavelength or Helmholtz resonators, etc. Therefore, examining these basic acoustic components from the angle of wave-velocity modulation might offer new perspectives, but the topic remains underexplored. This work examines the dispersion properties of an acoustic duct with branched acoustic resonators, alongside a transient experiment for sound speed quantification. It is shown that an acoustic resonator can lower both the phase and group velocities of acoustic waves below its resonant frequency, induce strong attenuation above resonance, and increase the phase velocity while maintaining low group velocity at higher frequencies. These trends are underpinned by the corresponding changes in the resonator's effective bulk modulus (decreasing, negative, and increasing in the three respective frequency ranges). The predicted physical phenomena are analyzed through numerical simulations and verified by experiments in both time and frequency domains. This research elucidates the slow-sound characteristics of an acoustic resonator, offering valuable insights for advancing innovations in acoustic design.

1. Introduction

Achieving broadband noise attenuation has been a long-lasting challenge in acoustics, pertinent to many applications. Traditional mufflers, such as absorbers embedding porous materials and micro-perforated panels, inherit narrow bandwidth and design limitations [1]. Likewise, impedance mismatch-based silencers are usually bulky, which hinders their practical deployment [2–3]. To overcome these shortcomings, acoustic metamaterial mufflers have gained considerable attention owing to their ability to combine broadband performance with compactness [4–6]. Metamaterials can exhibit exotic properties which are not attenable in nature materials, exemplified by negative mass density and bulk modulus within bandgaps [7–10]. Nonetheless, precise tuning of resonance coupling remains challenging, particularly in the presence of destructive interference or manufacturing inaccuracies [11].

As an emerging alternative, acoustic designs based on wave velocity manipulation offer new possibilities for realizing high performance acoustic devices. Notable examples include Sonic Black Hole (SBH) structures, known for their ability to slow sound speed, and Delay-Line Acoustic Metamaterial (DLAM), which emulates an expanded acoustic space by reducing sound speed [12]. Sonic Black Hole (SBH) designs [13–14] based on slow-sound effects, offer a pathway to slowing acoustic waves, compressing wavelengths, and accentuating energy, thereby attaining effective broadband absorption with reduced dependence on conventional damping materials

* Corresponding author.
E-mail address: li.cheng@polyu.edu.hk (L. Cheng).

https://doi.org/10.1016/j.wavemoti.2026.103812
Received 19 March 2026; Received in revised form 14 July 2026; Accepted 4 August 2026
Available online 6 August 2026
0165-2125/

[15–16].

The so-called "slow sound" has been exploited for manipulating sound waves [17–18], a phenomenon initially confirmed in various structures, including acoustic resonators [4,12], helical and subwavelength metamaterials [19–20], mesoscopic hybrid slit-resonator metamaterial [21], and meta-porous absorbers [22–25]. Since many of these complex structures can be regarded as assemblies of acoustic resonators (such as Quarter-wavelength resonators (QWR) and Helmholtz resonators (HR)), re-examining these basic acoustic components from slow-sound perspective offers a unique angle to understand the underlying wave-modulation mechanisms, which is crucial for designing broadband absorbers that leverage these phenomena [26]. Previous work mainly focused on the frequency range below the resonant frequency, while the potential of these units for wave speed manipulation in other frequency ranges has received little attention. Moreover, research in slow-sound effects has mostly been conducted in frequency domain (steady-state), with far fewer studies addressing time-domain behavior. One remarkable attempt made in time domain is the study on Delay-Line Acoustic Metamaterials [12], in which the transmission time of reflected waves in a waveguide, side-loaded with HRs, was measured, visualizing the slow-sound effect for the first time. However, quantifications of these effects in terms of both phase and group velocities and their physical implications remained obscure.

These gaps motivate the present research, which shows its novelty by targeting a three-fold objective: first, to establish a generic model to evaluate the wave-speed modulation capability of various types of acoustic resonators embedded in a waveguide; second, to systematically assess the wave speed variation across the entire frequency range and elucidate the underlying physical mechanisms; third, to develop a time-domain evaluation method and validate it alongside the salient slow-wave phenomena via transient experiments.

The reminder of the paper is structured as follows. In Section 2, a general model based on effective medium approach (EMA) is established to describe the wave speed variation of a resonator embedded in or side-loaded onto an acoustic waveguide, with the reflection-transmission inverse method (R-TIM) employed in parallel for validation. In Section 3, a side-loaded quarter-wavelength resonator (QWR) is used to demonstrate the variations of effective phase and group velocities in different frequency ranges. Theoretical analysis is then conducted and validated through both transient and steady-state simulations, with associated physical explanations provided. Similarities and differences with other types of resonators are also briefly discussed. Section 4 outlines the time-domain experimental setup and testing process, to verify the theoretical predictions in terms of phase and group velocity changes in a single QWR configuration. Conclusions are then summarized in Section 5. Details on analytical treatment and frequency-domain experiments are provided in Appendices for reference.

2. Theory and system modelling

A general effective medium approach (EMA) model for describing a single local resonator embedded in or side-loaded onto the acoustic waveguide with anechoic boundary is illustrated in Fig. 1. The left part presents the schematic of a two-dimensional waveguide, comprising air medium (gray regions at both ends). Both ends of the waveguide are assumed to satisfy non-reflective boundary conditions. Assuming a plane wave p_i incident upon the structure, the reflected wave p_r and transmitted wave p_t are generated, from which the reflection and transmission coefficients R and T are to be determined. Before the cut-on frequency of the wave guide, where the wavelength of the incident wave is much larger than the size of the structure, the acoustic structure (between the two air medium portions) can be treated as an effective medium layer. For QWR and HR, depending on the length of insertion h in the waveguide, they can be categorized as branched ($h = 0$) or partially inserted ($0 < h < H$), where H is the height of the duct. The acoustic medium corresponding to the narrowing portion of the duct is labeled A, with a thickness d, while the portion bounded by the

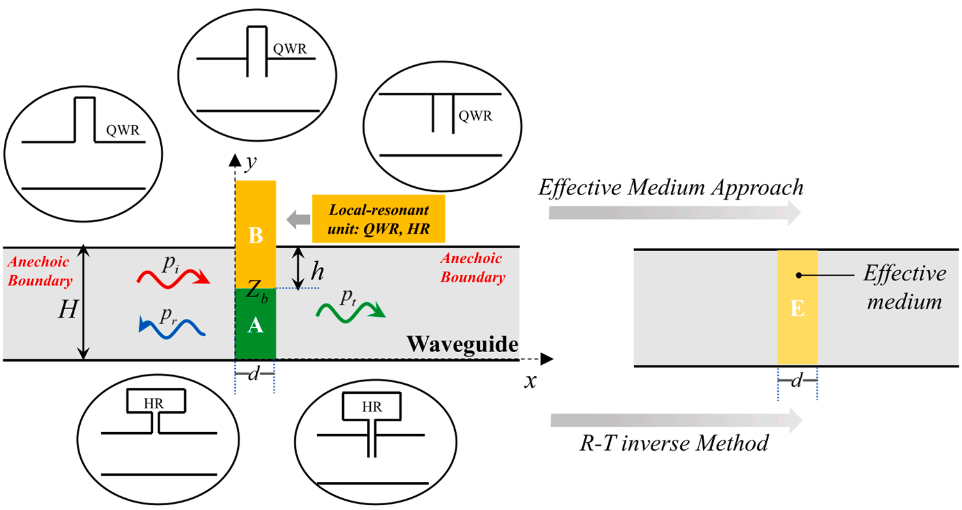

Fig. 1. A generic EMA model for an acoustic waveguide comprising various locally resonant units.

partition and the resonator is denoted by B. Under the above long-wavelength assumption, the combination of these two parts can be seen as an effective medium E. To understand the generic effect of damping in the proposed system, complex sound speed is assumed as $c_0 = 343(1+\xi j)$ m/s, where the imaginary part ξ denotes an isotropic loss factor. At the interface between A and B, the surface impedance of the area B, Z_b, depends on the specific type of the resonators. The acoustic wavenumber in medium A can be decomposed into two propagative components in x and y directions, respectively, as

$$k_A^2 = k_{A,x}^2 + k_{A,y}^2. \tag{1}$$

For harmonic waves, by ignoring the time-domain harmonic term $e^{j\omega t}$, the sound pressure field in medium A can be described as

$$p_A(x,y) = \left(C_y \cos k_{A,y} y + D_y \sin k_{A,y} y\right)\left(C_x e^{-jk_{A,x}x} + D_x e^{jk_{A,x}x}\right), \tag{2}$$

where C_x, C_y, D_x, D_y are undetermined amplitude coefficients of sound pressure. The above expression decomposes the acoustic waves as propagative along x and oscillatory along y. The acoustic velocity in y direction can be derived as

$$V_{A,y} = -\frac{\partial p_A(x,y)}{\partial y}\frac{1}{j\rho_0\omega}. \tag{3}$$

ρ_0 here denotes the mass density of the air; and ω the angular frequency. To satisfy the boundary condition along the rigid wall at $y=0$, $V_{A,y}=0$, Eq. (2) can be rearranged as

$$p_A(x,y) = C_y \cos k_{A,y} y\left[C_x e^{-jk_{A,x}x} + D_x e^{jk_{A,x}x}\right]. \tag{4}$$

At the interface between media A and B, i.e. $y = H-h$, $p_A(x,y) = Z_b V_{A,y}$, yielding

$$\cos\left(k_{A,y}(H-h)\right) = Z_b \frac{1}{j\rho\omega} k_{A,y} \sin\left(k_{A,y}(H-h)\right). \tag{5}$$

Rearranging Eq. (5) gives

$$k_{A,y} \tan k_{A,y}(H-h) = Z_b \frac{k_{A,y}}{j\rho\omega}. \tag{6}$$

Solving Eq. (6) for $k_{A,y}$ and combining Eq. (1), the effective wave number $k_{A,x}$ in the effective medium E can be obtained. The corresponding effective phase velocity and group velocity write, respectively

$$c_{ph} = \frac{\omega}{k_{A,x}}, c_g = \frac{d\omega}{dk_{A,x}}. \tag{7}$$

The density of the medium A equals to ρ_0, and the rigid partitions in the area B block the sound propagation in x direction, therefore the region B can be modeled as an effective medium with static anisotropic properties [22,27] as

$$\rho_B = \begin{bmatrix} \rho_{B,x} & \\ & \rho_{B,y} \end{bmatrix} = \begin{bmatrix} \infty & 0 \\ 0 & \rho_0 \end{bmatrix}. \tag{8}$$

The effective mass density of E in x direction can then be obtained from

$$\frac{1}{\rho_E} = \frac{1-\eta}{\rho_A} + \frac{\eta}{\rho_{B,x}}, \eta = \frac{h}{H}. \tag{9}$$

As $\rho_{B,x} = \infty$ (rigid partitions),

$$\rho_E = \frac{\rho_0}{(H-h)/H}. \tag{10}$$

According to the definition of air bulk modulus and characteristic impedance, the effective impedance and bulk modulus of medium E can be obtained as

$$Z_E = c_{ph}\rho_E, \tag{11}$$

$$\kappa_E = c_{ph} Z_E. \tag{12}$$

To validate the results obtained from the EMA model, the effective parameters derived from reflection-transmission inverse method (R-TIM) are briefly recalled [28–30]. The effective characteristic impedance of the medium E, Z_E, writes

$$Z_E = Z_0\sqrt{\frac{(1+R)^2 - T^2}{(1-R)^2 - T^2}}, \tag{13}$$

in which Z_0 is the characteristic impedance of the air, R and T are the reflection and transmission coefficients, respectively. The effective wavenumber k_E writes

$k_E = \frac{\ln|e^{jk_E d}|}{jd} + \frac{\arg(e^{jk_E d}) + 2\pi m}{d}$, (14) which is result from the inversion of

$$e^{jk_E d} = \frac{T(\zeta - 1)}{R(1+\zeta) - (1-\zeta)}, \zeta = \frac{Z_E}{Z_0}. \tag{15}$$

Here *arg* is the argument of a complex number, m is a natural integer used to correct the phase after inversion, which depends on the thickness d of the medium E in x direction, resulting from the multi-valued complex spoke angles. It should be noted that the present model is based on the plane-wave assumption. Therefore, in addition to the long-wavelength assumption, the effective sound speed predicted by the model should be regarded as reliable only below the first cut-off frequency of the duct.

3. Typical acoustic units

3.1. A branched QWR

The most common and straightforward case, QWR (branched), is discussed firstly to elucidate its slow-sound properties. Fig. 2 shows two methods for describing a branched QWR in the waveguide, TMM (Transfer Matrix Method) [31] and EMA. Here, TMM serves as a benchmark to verify the validity of EMA model in terms of the predicted Transmission Loss (TL). Since the derivation of TMM for a branched QWR is a well-established theory and not the primary contribution of this paper, the specific derivation is provided in Appendix. A1. In Fig. 2, d is the width of QWR, h_{QWR} is the height of the QWR, H is the height of the waveguide. The surface impedance at the QWR opening is

$$Z_{QWR} = -j\rho_0 c_0 \cot k_0 h_{QWR} + j\rho_0 c_0 k_0 \Delta L. \tag{16}$$

The length correction ΔL is commonly applied to account for the radiation effect at the interface between the QWR and the waveguide [32] as

$$\Delta L = 0.82\left[1 - 0.235\frac{d}{H} - 1.321\left(\frac{d}{H}\right)^2 + 1.54\left(\frac{d}{H}\right)^3 - 0.86\left(\frac{d}{H}\right)^4\right]d. \tag{17}$$

In the EMA model, taking $Z_b = Z_{QWR}$, the effective dispersion relationship derived from Eq. (6) for the effective medium E is given by

$$k_{A,y}\tan k_{A,y}H = (-jZ_0\cot k_0 h_{QWR} + jZ_0 k_0 \Delta L)\frac{k_{A,y}}{j\rho_0\omega}. \tag{18}$$

Since Eq. (18) is transcendental, a small-angle assumption is introduced to solve this equation,

$$\tan_{k_{A,y}H} \approx k_{A,y}H. \tag{19}$$

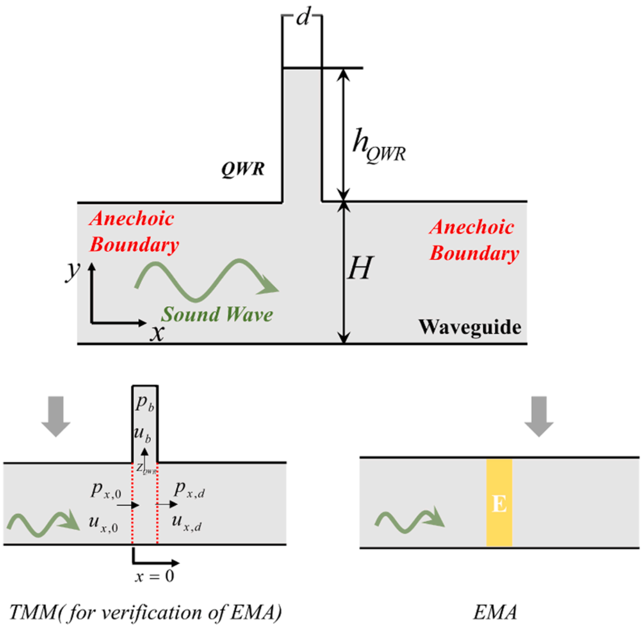

Fig. 2. Two methods (TMM, EMA) to describe a branched QWR in the waveguide.

This assumption is valid when the long wavelength assumption is met, [16,17,20,33]. Then, the effective wavenumber k_E can be obtained as

$$k_E = k_{A,x} = \sqrt{{k_0}^2 - \frac{k_0}{H}\left(\frac{1}{k_0\Delta L - \cot k_0 h_{QWR}}\right)}. \tag{20}$$

Other effective parameters can then be determined by using Eqs. (7), (10)-(12). The acoustic pressures and volumetric velocities at both ends of medium E are linked through the effective transfer matrix $\mathbf{T_E}$,

$$\begin{bmatrix} p_{x,0} \\ u_{x,0} \end{bmatrix} = \mathbf{T_E} \begin{bmatrix} p_{x,d} \\ u_{x,d} \end{bmatrix}, \tag{21}$$

$$\mathbf{T_E} = \begin{bmatrix} \cos k_E d & jZ_E \sin k_E d \\ \dfrac{j}{Z_E}\sin k_E d & \cos k_E d \end{bmatrix}. \tag{22}$$

The definition of Transmission Loss (TL) writes $TL = 20\log_{10}\frac{1}{T}$ where $T = p_t/p_i$ is the transmission coefficient. Calculation for the T can be achieved by

$$\mathbf{T} = \begin{bmatrix} T_{11} & T_{12} \\ T_{21} & T_{22} \end{bmatrix}, \quad T = \frac{2}{T_{11} + (T_{12}/Z_0) + Z_0 T_{21} + T_{22}}. \tag{23}$$

3.2. *Wave speed variation with a branched QWR*

Fig. 3(a) shows the TL of the duct with a branched QWR, which exhibits a peak at the first resonant frequency of the QWR, 1355 Hz.

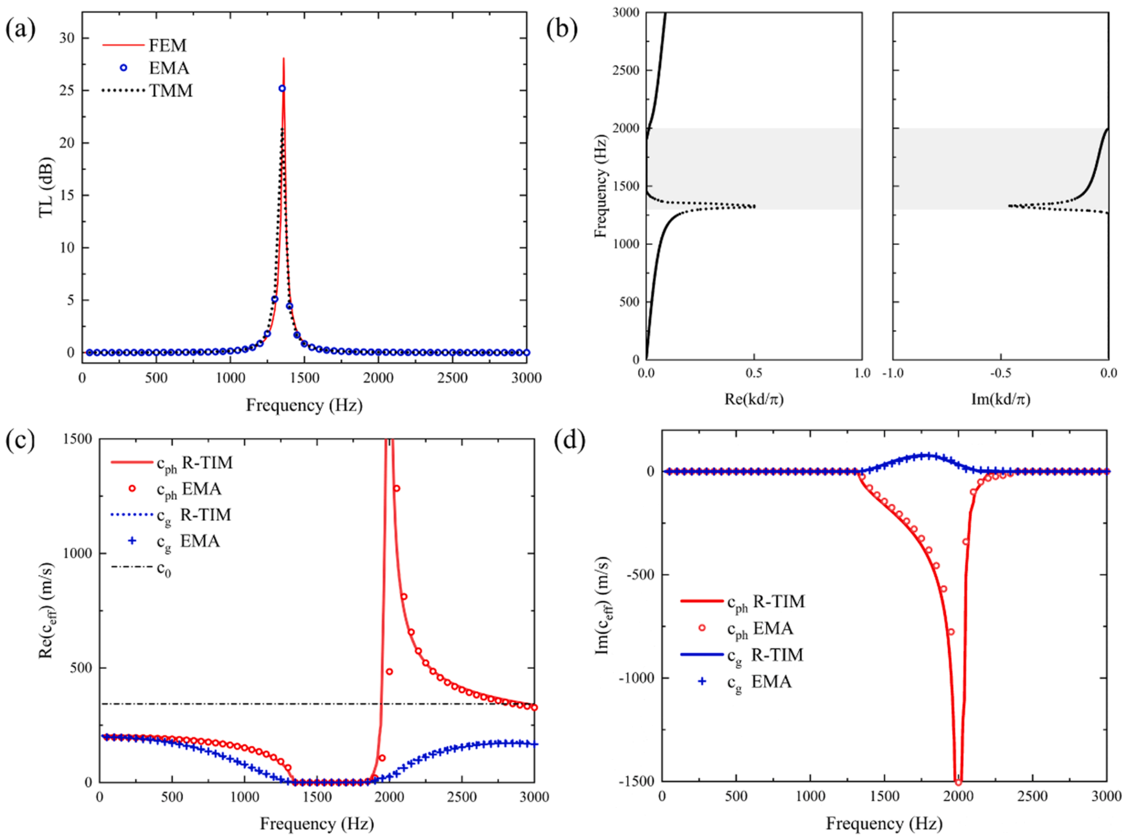

Fig. 3. (a) Transmission Loss (TL) calculated by FEM, EMA, and TMM. (b) Normalized dispersion relationship of the branched QWR, calculated by R-TIM, real part (left), and imaginary part (right). (c) Real part and (d) imaginary part of the effective group and phase velocities.

The parameters used in this case are:$H = 0.03$ m,$h_{QWR} = 0.06$ m,$d = 0.005$ m. Damping loss factor is taken as $\xi = 0.01$. We numerically model the branched QWR with a two-dimensional (2D) finite-element model using the pressure acoustics, frequency domain module of COMSOL Multiphysics software. The TL results from TMM, FEM, and EMA show good agreement with each other, indicating the correctness of the EMA model.

The dispersion relation of the duct with the branched QWR is shown in Fig. 3(b), obtained from R-TIM. The phase and group velocities, $c_{ph} = \omega/k(\omega)$ and $c_g = d\omega/dk(\omega)$, derived from the dispersion curve in Fig. 3(b), are shown in Figs. 3(c)-3(d), respectively, showing good agreement with the EMA results. As reference, the sound speed in air, (c_0, black dash-dot line) is also plotted for comparison.

As shown in the figures, the effective sound speed of the branched QWR can be roughly divided into three regions.

Region 1 (below the resonant frequency 1355 Hz): Both the group velocity (blue) and the phase velocity (red) are lower than c_0 and decrease to nearly zero when approaching the resonant frequency.

Region 2 (1355–2000 Hz): Close and slightly above the resonance, evanescent/near-field waves dominate, as indicated by the large imaginary part of the effective wavenumber in Fig. 3(b) (colored in gray). In this region, both phase/group velocities appear as pure imaginary, indicating that the sound waves are strongly attenuated during propagation.

Region 3 (above the resonant frequency 2000–2900 Hz): The group velocity remains lower than c_0, while the phase velocity exceeding it. Since the sound-energy-propagation speed corresponds to the group velocity, this indicates the presence of a slow-sound phenomenon in this region as well. Mathematically, although $n_{eff} = c_0/c_{ph} < 1$, the positive dispersion term $\omega dn_{eff}/d\omega$ is sufficiently large to give $\left(n_{eff} + \omega dn_{eff}/d\omega\right) = c_0/c_g > 1$, and hence $c_g < c_0$.

Further beyond 2900 Hz, the velocity variation returns to the pattern observed in Region 1, showing similar behavior before the second resonance of the QWR, which is not discussed further.

To verify the sound-speed variation observed in Fig. 3(c), nine time-domain cases at different frequencies are selected from three regions: 500 Hz and 1000 Hz (Region 1); 1355 Hz, 1500 Hz, and1700 Hz (Region 2); 2000 Hz, 2500 Hz and 2800 Hz (Region 3). Notably, 1355 Hz is the resonant frequency of the QWR.

Fig. 4 illustrates the schematic of the time-domain simulations conducted with and without the branched QWR. We numerically model the branched QWR with a two-dimensional (2D) finite-element model using the pressure acoustics, transient module of COMSOL Multiphysics software. Same as before, air is used as the medium in both the QWR and waveguide. Both cases are configured with anechoic boundaries (colored blue in Fig. 4(a)) and excited using a tone-burst signal (green wave arrow in Fig. 4(a)). Four simulation points, mimicking four microphone positions (the black dots indicated by the red arrow in Fig. 4(a)), are placed in pairs along the same x-coordinate to detect the original and modulated signals (blue wave arrow). By incorporating anechoic boundaries, this setup eliminates unwanted reflections that could affect the extraction of time delays. As an example, a 5-cycled 1000 Hz tone-burst signal in Fig. 4(b) is considered; the solid blue line represents the signal in time domain, the dashed line indicates its envelope, and the red line corresponds to the FFT results. Signal $S(t)$ features:

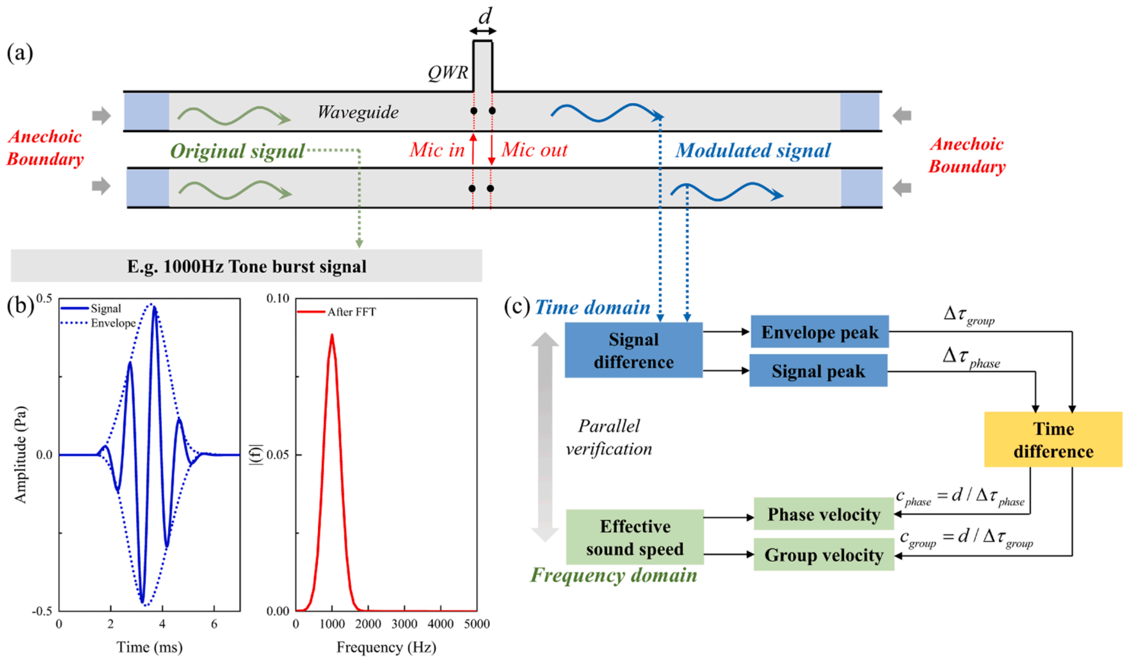

Fig. 4. (a) Schematic of the transient simulation. (b) Tone burst signal used in simulation (e.g., 1000 Hz), and FFT results. (c) Validation process of the effective speed in time domain.

$$S(t) = \sin(2\pi f t) e^{-\left(\frac{t-T}{T}\right)^2}, T = \frac{1}{f}, \tag{24}$$

where$f$is the center frequency.

The procedure for verifying the effective group and phase velocities is illustrated in a flowchart in Fig. 4(c). For a QWR of width d, the travel time of the signal over this distance d is evaluated as $\Delta\tau_{phase} = d/c_{phase}$ and $\Delta\tau_{group} = d/c_{group}$. The geometric parameters used in this transient simulation are the same as those shown in Fig. 3. Specifically, the phase and group velocities are identified as the propagation speeds of isophase and isoamplitude plane, respectively [34]. In transient simulations, the phase and group velocities are derived from the progression of the waveform peak and the envelope maxima, respectively. By extracting the time difference of sound wave propagating through the structure, the effective velocities can be determined.

Fig. 5(a) shows 1000 Hz tone-burst signals received by microphones at the inlet and outlet of the QWR. When the center frequency falls in Region 1, both the group and phase velocities decrease. The time difference marked by dark lines represents the propagation time associated with the group velocity, while the red line indicates the time corresponding to the phase velocity. Since air is a non-dispersive medium, the group velocity equals the phase velocity in a pure waveguide. Therefore, the isophase point and the signal envelope maxima take the same time to traverse an equal distance$d = 0.03$m, i.e., $\Delta\tau 1_{phase} = \Delta\tau 1_{group}$. After adding the branched QWR, the propagation time of both the isophase point and envelope maxima becomes significantly longer than that in a pure waveguide without QWR, indicating that the effective phase and group velocities are lower than c_0. The waveform distortion observed at the QWR outlet results from reflection and dispersion. A similar deformation occurs in Fig. 5(b), which will not be reiterated hereafter.

Region 3 is examined using a 2200 Hz tone-burst excitation. Fig. 5(b) shows that, after introducing the branched QWR, the travel time of the isophase point decreases, whereas that of the envelope motion increases significantly compared with the pure waveguide. This indicates that the effective phase velocity becomes higher than c_0, while the group velocity is lower than c_0. For Regions 1 and 3, the effective velocities obtained from characteristic points in both time and frequency domains are summarized in Fig. 6.

As shown in Fig. 6, the sound speed in the waveguide without QWR is fixed at 344.8 m/s (dashed black line). For the waveguide with a branched QWR at 500 Hz and 1000 Hz, the relative c_{ph} and c_g are lower than c_0. Due to the consistency between the frequency and time domain results, the following analysis is conducted using the time-domain results. As the frequency increases from 500 Hz to 1000 Hz, c_{ph} decreases from 164.8 m/s to 123.5 m/s, while c_g decreases from 156.3 m/s to 90.1 m/s. As the frequency approaches the resonant frequency, 1355 Hz, both velocities are further reduced. At the same frequency, $c_g < c_{ph}$, verifying the phenomenon shown in Region 1 of Fig. 3(c).

However, at 2000 Hz, 2200 Hz, 2500 Hz, and 2800 Hz, (Region 3), c_{ph} exceeds c_0, whereas c_g is lower than c_0. As the frequency rises, the effective phase velocity gradually decreases while the group velocity increases. The greatest discrepancy between the transient and steady-state results occurs at 2000 Hz, mainly because the finite bandwidth of the tone-burst signal spans the transition between Regions 2 and 3. Below 2000 Hz, the transmitted wave is attenuated, whereas components above 2000 Hz can propagate through the structure. Furthermore, near this transition, the effective wavenumber k_{eff} is small and varies rapidly with frequency. Since $c_{ph} = \omega/k_{eff}$, even a slight spectral shift can cause a large variation in the extracted phase velocity. Therefore, the remaining discrepancy at 2000 Hz reflects the high sensitivity of the velocity extraction near the transition rather than a contradiction between the transient and frequency-domain results.

In Region 2, exemplified by the 1355 Hz transient simulation (Fig. 7(a)), the acoustic wave is unable to maintain its original waveform. Near this resonant frequency, the acoustic wave is almost fully reflected, as indicated by its sound pressure field. At 1500 Hz and 1700 Hz, the attenuation of the sound wave becomes less evident due to the short dissipation length of a single QWR (0.005 m)

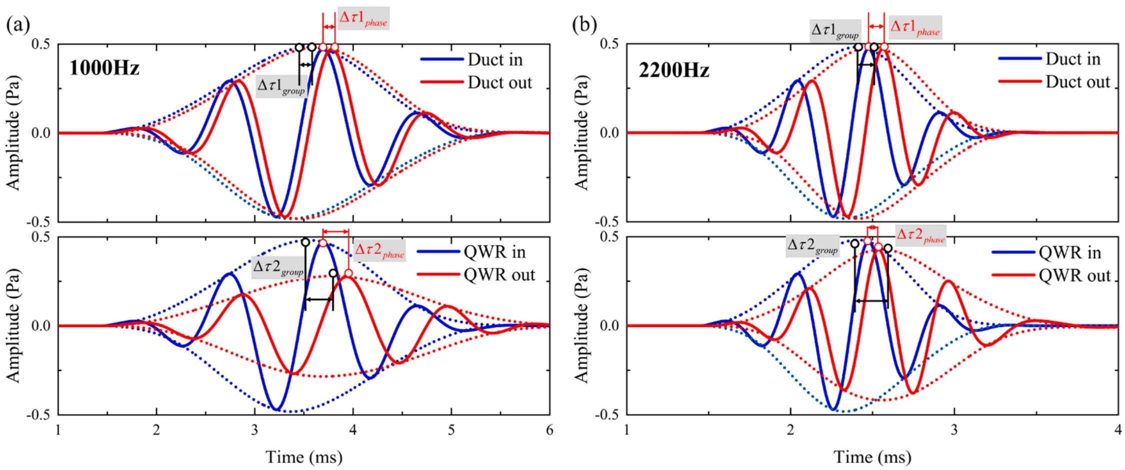

Fig. 5. Time-domain-simulation results: (a) 1000 Hz tone-burst signal, and (b) 2200 Hz tone-burst signal.

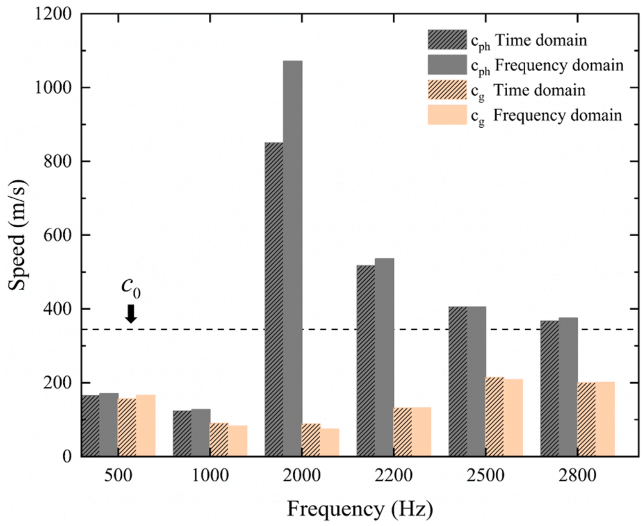

Fig. 6. Comparison of effective velocities obtained from both time and frequency domains.

which compared to the wavelength ($\lambda = 343/1700 \approx 0.2$m). To better visualize the effect, we put several identical QWR side-by-side (N = 10, 20, 50), so that the wavelength of the sound wave starts to match the dimensions of the aggregated structure. The corresponding TL curves in Fig. 7(d) are consistent with the pressure-field results: the TL peak near resonance corresponds to the strong reflection at 1355 Hz, while the enhanced and broadened TL for larger N agrees with the stronger wave attenuation observed in the pressure fields.

In Regions 1 and 3, similar steady-state simulation analyses can also be conducted. Two representative frequencies, 1000 Hz and 2200 Hz, are chosen for comparison to demonstrate wavelength compression/stretching and energy-focusing effects. As this study

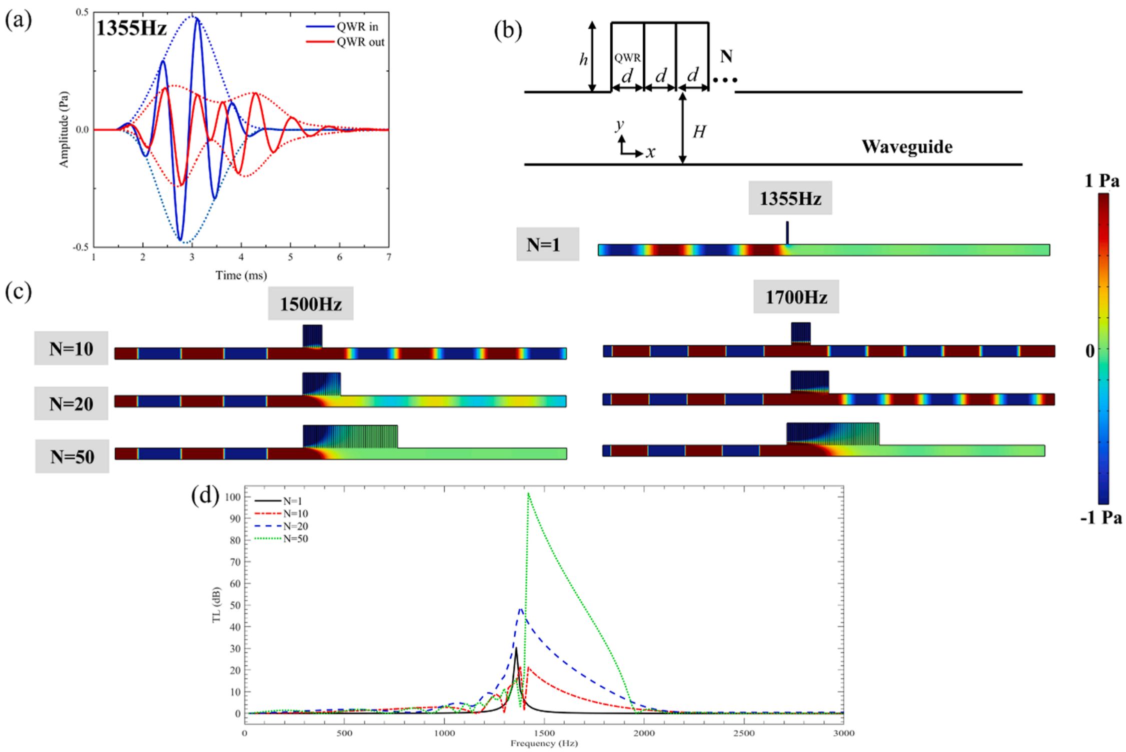

Fig. 7. Explanation for the effective velocities with purely imaginary parts. (a) Transient results of the 1355 Hz tone burst. (b) Schematic of the multiple-branched QWRs and pressure field of 1355 Hz, N = 1. (c) Pressure field of multiple QWRs at 1500 Hz and 1700 Hz. (d) TL performance of N = 1,10,20, and 50 QWRs.

primarily focuses on the wave-modulation capability of a single resonator, the details are presented in Fig. A2.

3.3. Effective parameter variation of a branched QWR

The effective bulk modulus and mass density of the duct-QWR portion are shown in Fig. 8 (calculated by the R-TIM). The relationship between the effective phase velocity c_{ph}, bulk modulusκ_E, and mass densityρ_E writes:

$$c_{ph} = \sqrt{\frac{\kappa_E}{\rho_E}}, \tag{25}$$

in which $\kappa_E$and$\rho_E$can also be divided into three regions.

Region 1: Both the effective bulk modulus and mass density are positive. As the frequency approaches the resonance, κ_E decreases, and $\rho_E = \rho_0$, resulting in $c_{ph} < c_0$. At the resonant frequency, ρ_E undergoes an abrupt change but remains positive, whereas $\kappa_E = 0$, leading to a zero value of c_{ph}.

Region 2: κ_E becomes negative, while $\rho_E = \rho_0$ remains constant. Consequently, c_{ph} is purely imaginary, indicating strong attenuation and rapid decay of the acoustic wave. The abrupt change of κ_E at 2000 Hz leads to the infinite value of c_{ph} in Fig. 3(c).

Region 3: Above 2000 Hz, $\kappa_E > \kappa_0$, ρ_E remains unchanged, resulting in $c_{ph} > c_0$. As the frequency continues to increase, the system returns to Region 1, which is consistent with the phenomenon shown in Fig. 3(c).

3.4. Partially inserted, inserted QWR

Gradually increasing the insertion h (which is mentioned in Fig. 1) leads to a configuration change from branched to partially inserted. The general EMA model, still applicable, requires slight changes as the insertion depth increases:

1) The lowest resonant frequency of the inserted resonator is limited. As shown in Fig. 9(b), the longest QWR is $h_{qwr} = H$, so the lowest resonant frequency can be approximated as $f_c = c_0/4H$. 2) The effective mass density is no longer equal to the air density ρ_0 but depends on the insertion length h, which can be calculated using Eq. (10). 3) As the insertion increases from $h = 0$ to $h = h_{qwr}$, the near-field effect becomes more pronounced, challenging the plane-wave assumption around the resonator.

The steady-state simulation results calculated by COMSOL are shown in Fig. 9(a), depicting the acoustic pressure field along the y-direction at 0.001 m from the right side of the unit (black dashed line) at 2000 Hz. The height of duct H is 0.03 m, $h_{qwr} = 0.028$m, and $d = 0.005$m. When $h = 0$ (branched), the acoustic pressure distribution approximately satisfies the plane wave assumption. For $h = 0.5 * h_{qwr}$(partially inserted), the y-direction field deviates from the plane wave, and the near-field effect is even more significant when $h = h_{qwr}$ (inserted). Therefore, when calculating the TL of the inserted QWR, a correction needs to be applied. The required correction transfer matrix for the near-field effect is given as follows [35],

$$\mathbf{T}_{\text{correction}} = \begin{bmatrix} 1 & j\omega M_a \\ 0 & 1 \end{bmatrix}, M_a = -\frac{2\rho_0}{\pi}\ln\left(\sin\left(\pi\frac{H-h}{2H}\right)\right). \tag{26}$$

Fig. 9(b) compares the TL of an inserted QWR ($d = 0.005$m, $H = 0.03$m, $h = 0.024$m) before and after applying the near-field corrections with EMA, along with FEM results. The TL obtained by EMA after near-field correction agrees better with FEM.

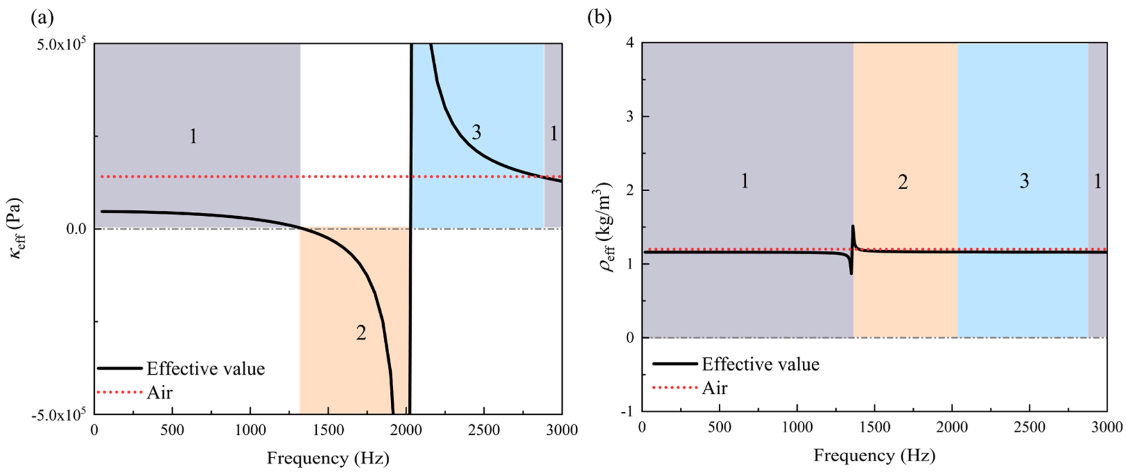

Fig. 8. (a) Effective bulk modulus and (b) mass density of a branched QWR. The black solid line represents the modulus and mass density of air, the red dash-dotted line represents the reference zero value, and the blue solid-point line represents the effective value.

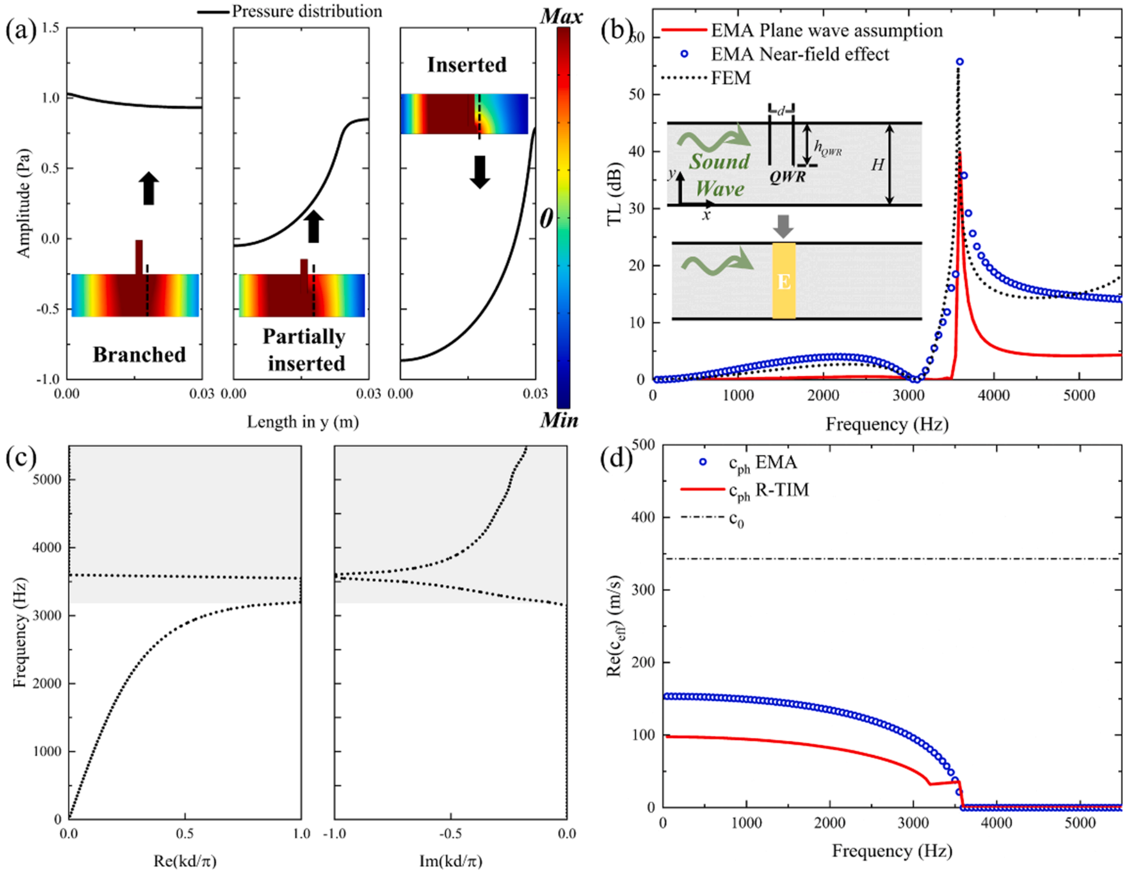

Fig. 9. (a) Near-field pressure distribution of a branched, partially inserted, inserted QWR. (b) TL of the inserted QWR calculated by EMA (with plane wave assumption), EMA (considering near-filed effect), and FEM results. (c) Normalized dispersion relationship of the inserted QWR, calculated by R-TIM, real part (left), and imaginary part (right). (d) The real part of the effective phase velocity of an inserted QWR.

Fig. 9(c) shows the dispersion relationship of an inserted QWR using R-TIM. The folding region in Fig. 9(c) (3200–3580 Hz), different from that of the branched QWR, is also highly dissipative, as evidenced by the imaginary part, consistent with a similar phenomenon reported for HR [12]. Fig.9(d) shows the real part of the effective phase velocity, calculated using both the EMA and R-TIM. The black dash-dot line in Fig. 9(d) represents the sound speed in the air. Since the R-TIM accounts for the near-field effect while the EMA method does not, discrepancies exist between the two sets of results. Nevertheless, the primary trend predicted by both EMA and R-TIM is consistent. Below the resonance frequency 3580 Hz (Region 1), the effective phase velocity is reduced like the branched QWR. After the resonance frequency, the effective speeds are purely imaginary (Region 2). Since frequencies above 5500 Hz are very close to the duct cut-off frequency (5715 Hz in this case), Region 3 is not shown in Fig. 9(d).

By replacing the QWR with HR, the effective sound speed can also be described using the EMA model. The primary difference between a branched QWR and HR is that Z_b in the Eq. (6) needs to be reconsidered, leading to different relative dispersion relation. Due to the complex form of Z_b for the HR, exact expressions are given in Appendix A2. Once Z_b is used in Eq. (6), the effective phase and group velocities can be obtained. Since the effective dispersion relationship of the HR is similar to that of the QWR, the corresponding results are not further discussed here, and given in Appendix D.

4. Experimental verifications

Experimental verifications are conducted using both time-domain and frequency-domain approaches, corresponding to the transient simulations and the R-TIM, respectively. Compared with the frequency-domain experiments, the transient experiments provide a clearer demonstration of wave-speed modulation, and the corresponding methodology and results constitute the main contribution of this work. Accordingly, the main text focuses on the transient experiments, while the setup and results of the frequency-domain experiments are provided in Appendix C.

Fig. 10 depicts the experimental setup for the time-domain measurements using a single QWR configuration. The basic principles are consistent with those shown in Fig. 4(c). The system consists of a signal generator (KEYSIGHT-33500B, producing a tone-burst signal), a power amplifier (B&K-2706, boosting the signal voltage), an impedance tube system (BSWA-4601, comprising a

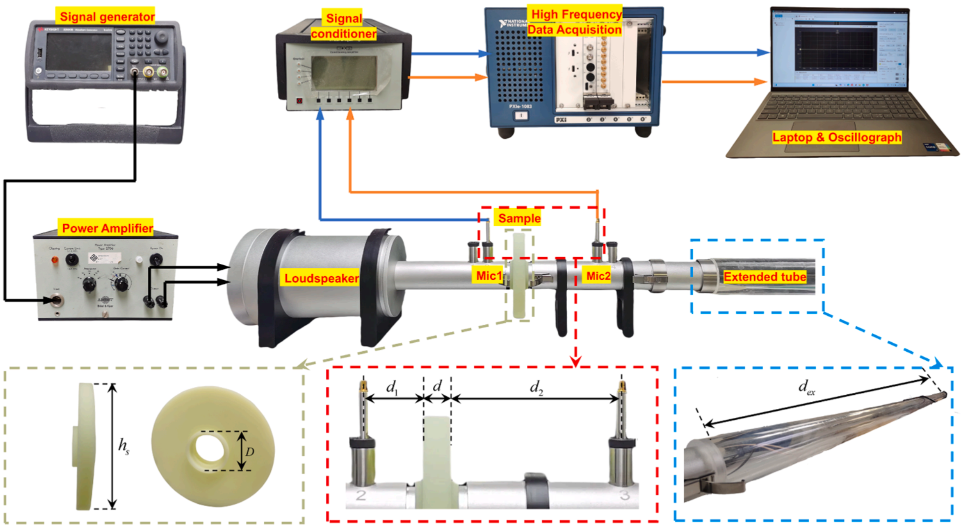

Fig. 10. The schematic of the transient experiment.

loudspeaker to generate the signal), two microphones (B&K-4958), an additional extended duct, a signal conditioner (B&K-1704, calibrating microphone sensitivity and adapting data acquisition), a high-sampling-rate data acquisition system (NI-PXle-1083, ensuring sufficiently small sampling intervals to capture the wave-speed-manipulation ability of a single resonator), and a computer with an integrated oscilloscope (to observe the waveform received by the microphones).

The experiment employs a 10-cycle tone-burst signal to make the central frequency as prominent as possible. Since the characteristic of the signals have already been analyzed in Fig. 4(b), the illustrations of the relevant waveforms are not provided. Expression of the signal writes

$$S(t) = \sin(2\pi ft)[1 - \cos(2\pi ft / 10)], T = \frac{1}{f}. \tag{27}$$

The meaning of parameters are the same as those in Eq. (24).

Because accurate measurement of the time difference between signal peaks is required, eliminating the effect of reflected waves becomes important. To this end, an extended duct is attached to the end of the impedance tube to distinguish the direct signal measured by the microphone from the reflected waves. The length of the extended tube depends on the total duration of the lowest frequency signal. The signal with the lowest frequency has the longest wavelength, thus requiring the greatest propagation distance to separate both waves. For example, at 500 Hz, the propagation distance required for a 10-cycle signal to pass a fixed point is $1\ /500 \cdot 343 \cdot 10/2\ = 3.43$m. Considering the distance from Mic2 to the extended duct, a 3-meter-long duct is sufficient to meet the experimental requirements. Additional sensitivity tests using tone-burst signals with different numbers of cycles confirmed that the 10-cycle signal provides a suitable compromise between frequency selectivity and the separation of direct and reflected waves and is therefore adopted in the present experiment. Table 1 tabulates the major parameters of the experimental setup.

A 3D-printed branched QWR is selected to evaluate its wave-speed modulation capability. The time difference between the signals received from the 1st and 2nd planes of the sample is $t_{measure}$; however, the actual time difference between Mic1 and Mic 2 is t_{total}. The two are related by

$$t_{measure} = t_{total} - \frac{d_1}{c_0} - \frac{d_2}{c_0}, \tag{28}$$

and the measured effective speed is

$$c_{measure} = \frac{d}{t_{measure}}. \tag{29}$$

Table 1
Meaning of the parameters in Fig. 10 and the sample parameters used in the experiment.

Name	d	d_1	d_2	h_s	D	d_{ex}
Meaning	Width of the sample	Length between the sample 1st plane and Mic1	Length between the sample 2nd plane and Mic2	Height of the sample	Diameter of the impedance tube	Length of the extended duct
Value (m)	0.010	0.035	0.10	0.109	0.029	3

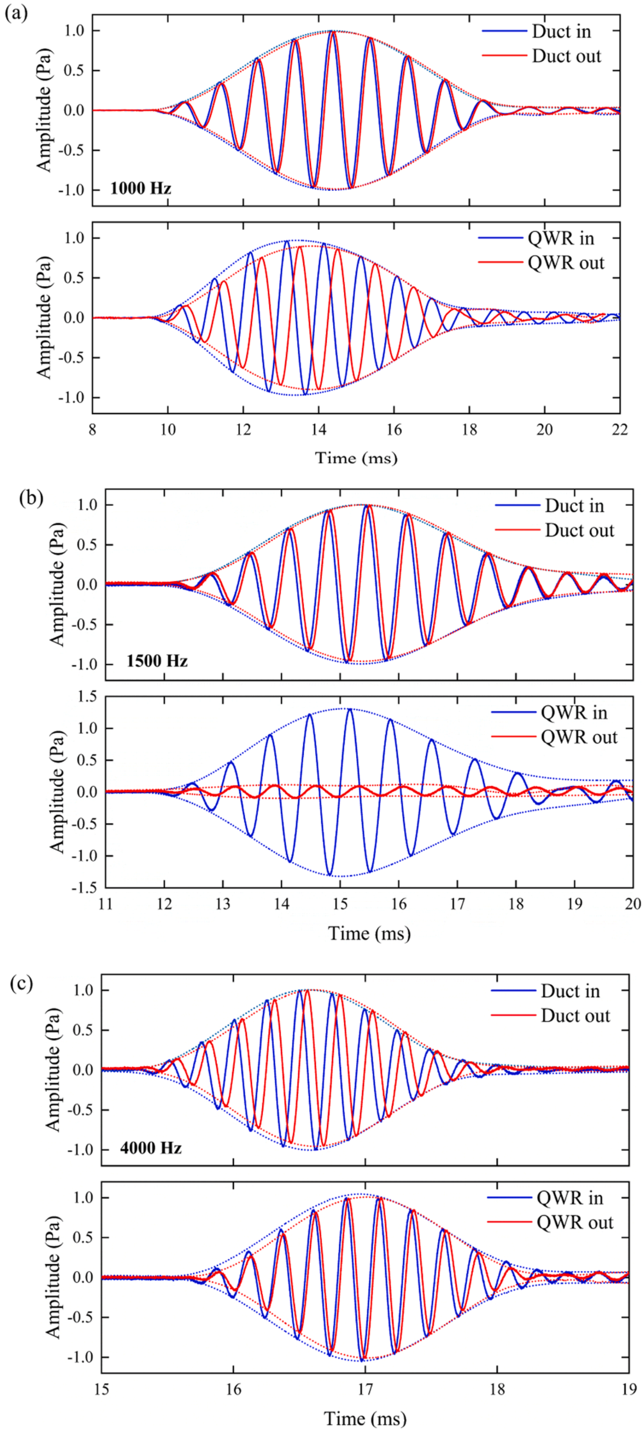

Fig. 11. Transient experimental results. (a-c) Transmitted signals in the duct with and without the QWR for center frequencies of 1000, 1550, and 4000 Hz, respectively.

The experiment is measured by using tone-burst signals with different center frequencies, ranging from 500–1550 Hz and 3800–5000 Hz in 50 Hz intervals.

Experimental results at the selected frequencies of 1000 Hz (Region 1), 1550 Hz (the resonant frequency), and 4000 Hz (Region 3) are given in Fig. 11. As shown in Fig. 11(a), the phase and group velocities are inferred by tracking the isophase points and the envelope peaks of the measured waveforms and comparing the corresponding travel times over the same propagation distance in a pure

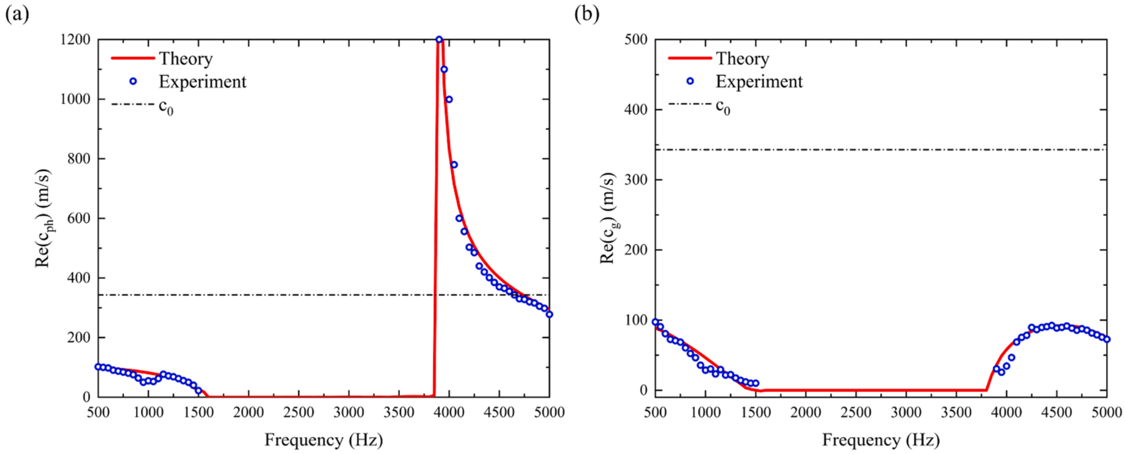

Fig. 12. (a) and (b) Comparison of the effective phase and group velocities achieved by transient experiment and theory.

duct and the duct with a QWR. At 1000 Hz, both the isophase points and the envelope peaks exhibit longer travel times than in the pure duct, indicating reductions in both phase and group velocities. At 1550 Hz, total reflection is observed. At 4000 Hz, the isophase points arrive earlier than in the pure duct, whereas the envelope peaks arrive later, implying an increased phase velocity but a decreased group velocity. The tails of all signals are not smooth, which is due to unavoidable reflections in the experiment. Besides this, all these observations are consistent with the time-domain simulation results shown in Figs. 5 and 7(a); therefore, no further discussion is provided here. An additional time-windowing analysis confirmed that the residual oscillations have only a minor influence on the extracted velocities and do not affect the main conclusions.

The time differences between the peaks of the wave packet and the envelope are compared, and the effective phase and group velocities are derived using Eq. (29), shown in Fig. 12 (blue circle). Theoretical results calculated by R-TIM (red line) are also given. The results show that both the overall trend and values of the experimental results align well with theoretical predictions. This agreement confirms the two distinct frequency ranges in which a single resonator can simultaneously slow down both the group and phase velocities of sound waves, as well as increase the phase velocity while reducing the group velocity.

5. Conclusions

This study presents a systematic investigation of the wave speed manipulation capabilities of an individual acoustic resonator. A general model based on effective medium approach (EMA) is established to capture the slow-sound effect of a resonator in the acoustic duct, which is verified with reflection-transmission inverse method (R-TIM). Using a branched Quarter-Wavelength Resonator (QWR) as an example, the effective dispersion relation and variations in phase and group velocities of sound waves are elucidated. These theoretical predictions are validated through simulations and experiments in both time and frequency domains. In this process, a time-domain experiment is proposed for the first time to extract and quantify the effective phase and group velocities of acoustic waves. The study also elucidates the similarities and differences among various resonators for the perspective of slow-sound effect. The following conclusions are drawn:

1) The generalized EMA model predicts the slow-sound phenomenon of resonators, regardless of the type (QWR or HR) and installation configurations (branched or partially inserted). All the units can slow both the group and phase velocities of incoming sound waves in the low-frequency region before their resonant frequencies. Close to the resonant frequency, the transmitted sound is strongly attenuated. As the frequency increases further, the phase velocity increases while the group velocity decreases. These trends are consistent with the corresponding changes in resonator's effective bulk modulus.
2) By identifying the isophase surfaces and envelope maxima of acoustic waves, a time-domain method is developed to extract the phase and group velocities of the propagating waves in the duct. This approach is validated through simulations and experiments, thereby providing a quantitative tool for characterizing the slow-sound effect in the time domain.
3) The slow-sound effects measured in both time-domain and frequency-domain experiments agree well with the theoretical predictions, further verifying the validity of the theoretical and numerical analyses. Notably, the separation and quantitative identification of the effective phase and group velocities in the time-domain experiment are reported for the first time.

In summary, this work establishes a unified framework for characterizing and exploring slow-sound phenomena of acoustic resonators in a waveguide, providing a robust theoretical basis for the manipulation of acoustic waves. The findings presented here are expected to inform the design of sound absorbers, wave-manipulation structures, and other advanced acoustic devices.

CRediT authorship contribution statement

Jinze Li: Writing – original draft, Visualization, Validation, Methodology, Formal analysis, Data curation, Conceptualization. **Xiang Yu:** Supervision, Methodology, Investigation, Conceptualization. **Li Cheng:** Writing – review & editing, Supervision, Resources, Project administration, Investigation, Funding acquisition, Conceptualization.

Declaration of competing interest

The authors declare that they have no known competing financial interests or personal relationships that could have appeared to influence the work reported in this paper.

Acknowledgements

Li Jinze acknowledges the insightful discussions with Dr. An Shuowei.

Appendix A. Analytical derivations

A.1 TMM derivation of a single QWR

Referring to Fig. 2, under the plane-wave assumption, the acoustic pressure at $x = 0$ and $x = d$ writes

$$p_{x,0} = C + D, p_{x,d} = Ce^{-jk_0 d} + De^{jk_0 d}. \tag{30}$$

In the above expression, C and D are the amplitudes of the incident and reflected waves, respectively. j is the imaginary unit, k_0 is the acoustic wave number in air. The volumetric velocity at $x = 0$is

$$u_{x,0} = S_{ex} v_{x,0} = S_{ex} \frac{C - D}{\rho_0 c_0}, \tag{31}$$

where $v_{x,0}$ is the particle velocity at $x = 0$, ρ_0 is the air density, c_0 is the sound speed in air, and S_{ex} is the cross-section area of the waveguide. The downstream volume velocity can be decomposed into two components based on the law of mass conservation. One part corresponds to the volumetric velocity u_b flowing into the QWR, while the other part $u_{x,d}$ remains in the waveguide. The volumetric velocity u_b can be expressed as

$$u_b = S_b v_b = S_b \frac{p_b}{Z_{QWR}}, \tag{32}$$

in which S_b, v_b, and Z_{QWR} are the area, particle velocity, and the surface impedance at the QWR opening. Specifically, considering that d is much smaller than the acoustic wavelength, sound pressure p_b at the QWR opening can be approximated by $p_{x,d}$. Finally, one can obtain the final transfer matrix $\mathbf{T_{QWR}}$ which relates the acoustic pressures and volumetric velocities at the inlet and the outlet of the QWR-affected region.

$$\begin{bmatrix} p_{x,0} \\ u_{x,0} \end{bmatrix} = \mathbf{T_{QWR}} \begin{bmatrix} p_{x,d} \\ u_{x,d} \end{bmatrix}, \tag{33}$$

where

$$\mathbf{T_{QWR}} = \begin{bmatrix} \cos k_0 d & \dfrac{j\rho_0 c_0 \sin k_0 d}{S_{ex}} \\ \dfrac{j\sin(k_0 d) S_{ex}}{\rho_0 c_0} & \cos k_0 d \end{bmatrix} \begin{bmatrix} 1 & 0 \\ \dfrac{S_b}{Z_{QWR}} & 1 \end{bmatrix}. \tag{34}$$

A.2 The surface impedance of HR

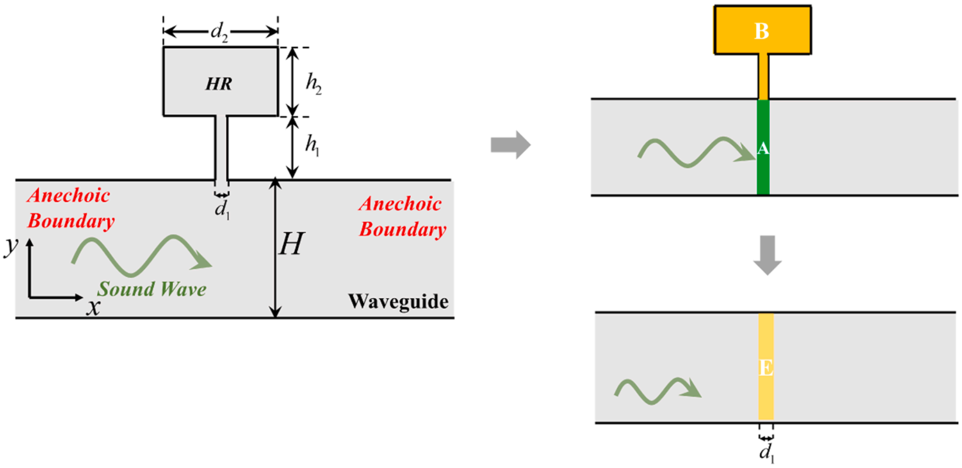

Fig. A1. The schematic of a branched HR by EMA model.

The surface impedance of a branched HR can be written as,

$$
\begin{aligned}
&Z_{HR} = \frac{r_{11}}{r_{21}},\\
&r_{11} = \cos kh_1 \cos kh_2 - (k\Delta L_1 + k\Delta L_2)\frac{S_c}{S_n}\cos kh_1 \sin kh_2 +\\
&(k\Delta L_1 + k\Delta L_2 - 1)\frac{S_c}{S_n}\sin kh_1 \sin kh_2 - k\Delta L_1 \cos kh_2 \sin kh_1 \frac{S_c}{S_n},\\
&r_{12} = \frac{j\sin kh_1}{Z_0}\cos kh_2 - k\Delta L_2 \sin kh_2 \frac{S_c}{S_n}\frac{j\sin kh_1}{Z_0} + \frac{j\sin kh_2}{Z_0}\frac{S_c}{S_n}\cos kh_1.
\end{aligned}
\tag{35}
$$

in which h_1, d_1, S_n, are the length, width, and cross-section area of the neck. h_2, d_2, and S_c have the same meanings for the cavity.ΛL_1,ΛL_2 account for the radiation at the discontinuity between the neck and the cavity [35], the neck and the waveguide [32].

$$
\begin{aligned}
&\Delta L_1 = 0.82\left[1 - 0.235\frac{d_1}{H} - 1.321\left(\frac{d_1}{H}\right)^2 + 1.54\left(\frac{d_1}{H}\right)^3 - 0.86\left(\frac{d_1}{H}\right)^4\right]d_1,\\
&\Delta L_2 = 0.82\left[1 - 1.35\frac{d_1}{d_2} + 0.31\left(\frac{d_1}{d_2}\right)^3\right]d_1.
\end{aligned}
\tag{36}
$$

A.3 Detailed effective wavenumber expressions of the different resonators. Effective wavenumber k_E of different resonators can be obtained by substituting the corresponding surface impedance Z_b of the QWR or HR and considering the insertion depth h of the partition by using Eq. (6). The detailed expressions are provided hereafter.

1) Partially inserted QWR:

$$
k_E = \sqrt{k_0^2 - \frac{k_0}{(H-h)[k_0\Delta L - \cot(k_0 h_{QWR})]}}.
\tag{37}
$$

2) Inserted QWR:

$$
k_E = \sqrt{k_0^2 - \frac{k_0}{(H-h_{QWR})[k_0\Delta L - \cot(k_0 h_{QWR})]}}.
\tag{38}
$$

3) Branched HR:

$$k_E = \sqrt{k_0^2 - \frac{jZ_0k_0}{HZ_{HR}}}. \tag{39}$$

4) Partially inserted HR:

$$k_E = \sqrt{k_0^2 - \frac{jZ_0k_0}{(H-h)Z_{HR}}}. \tag{40}$$

Appendix B. Wavelength compression/stretching and energy-focusing

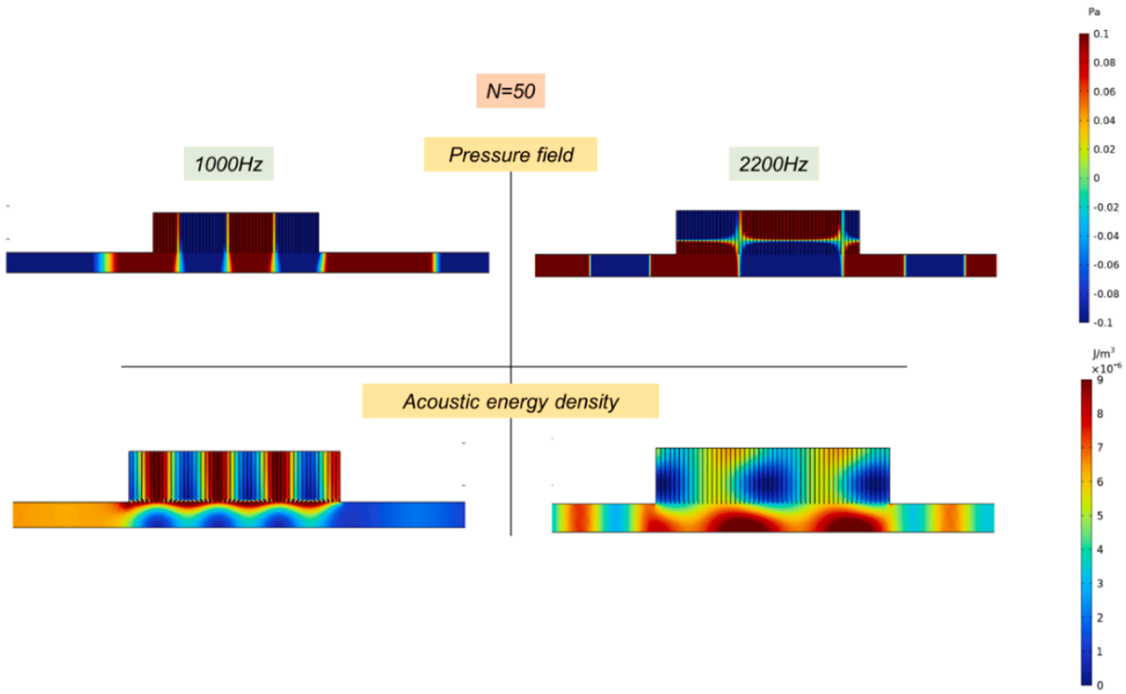

Fig. A2. Pressure field and acoustic energy density of branched QWRs at 1000 Hz and 2200 Hz.

Similar to the analysis in Fig. 7(c), steady-state simulation analyses for multiple QWRs with the same geometry can also be conducted for 1000 Hz (Region 1) and 2200 Hz (Region 3). The pressure field and energy density are provided to observe the wavelength and acoustic energy variations. Here, the acoustic energy density ε [36] is defined as;

$$\varepsilon = \frac{1}{2}\rho_0\left(v^2 + \frac{p^2}{\rho_0^2c_0^2}\right), \tag{41}$$

where p is the acoustic pressure; ρ_0 the air density; c_0 the speed of sound in air, and v the particle velocity. At 1000 Hz, the wavelength in the QWR-influenced region is significantly smaller than the wavelength in the external waveguide, indicating that the wavelength λ is compressed. At the same time, the acoustic energy density is significantly higher than that of the external waveguide, which corresponds to the reduced group velocity phenomenon. At 2200 Hz, the acoustic wavelength is obviously larger than that in the waveguide, which corresponds to the faster phase velocityc_0, while the acoustic energy density is still higher than that in the waveguide.

Appendix C. Frequency-domain experiment for verifying the effective speed using a branched QWR

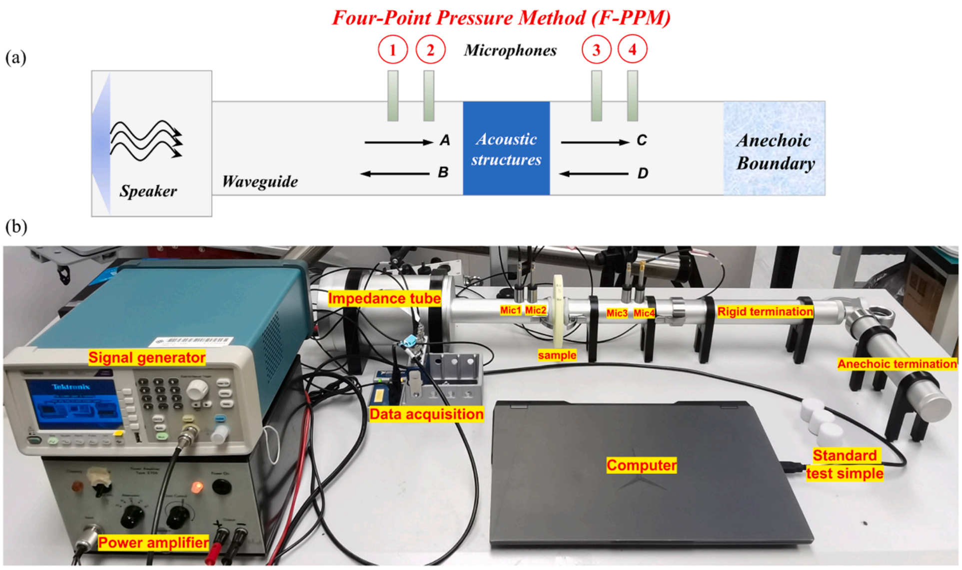

Fig. A3. (a) Schematic of the F-PPM to measure the reflection and transmission coefficients. (b) Frequency-domain experiment setup.

In addition to the time-domain experiment, the Four-point Pressure Method (F-PPM) is also used to measure the transmission and reflection coefficients of the structure [37,38], as shown in Fig. A3. The R-TIM is then employed to obtain its effective parameters. This part of the experiment verifies the wave speed modulation capability of a single acoustic resonator from the frequency domain perspective. The parameters of the sample have been listed in Table 1. As shown in Fig. A4, the results of the frequency-domain experiments also agree very well with the theoretical results.

These results provide further steady-state evidence of the slow-sound effect and, together with Appendix B, demonstrate wavelength modulation and acoustic energy concentration within the QWR-influenced region.

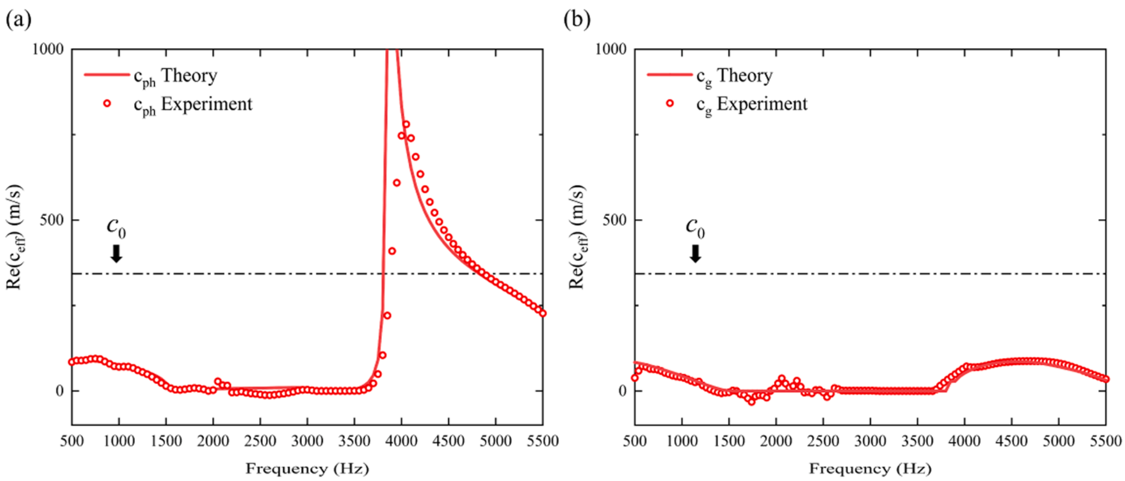

Fig. A4. The effective phase velocity calculated in theory and frequency-domain experiment. (a-b) the effective phase and group velocity of the sample.

Appendix D. Wave speed variation with a branched HR

Analyses show that HR also feature wave-speed modulation characteristics, highly similar to those of the QWR. Corresponding parameter changes are shown in Fig.A5. The geometric parameters of the HR used in this case are $H = 0.03$m, $h_1 = 0.02$m, $h_2 = 0.03$m, $d_1 = 0.005$m, and $d_2 = 0.03$m. The meaning of these parameters can be found in Fig.A1.

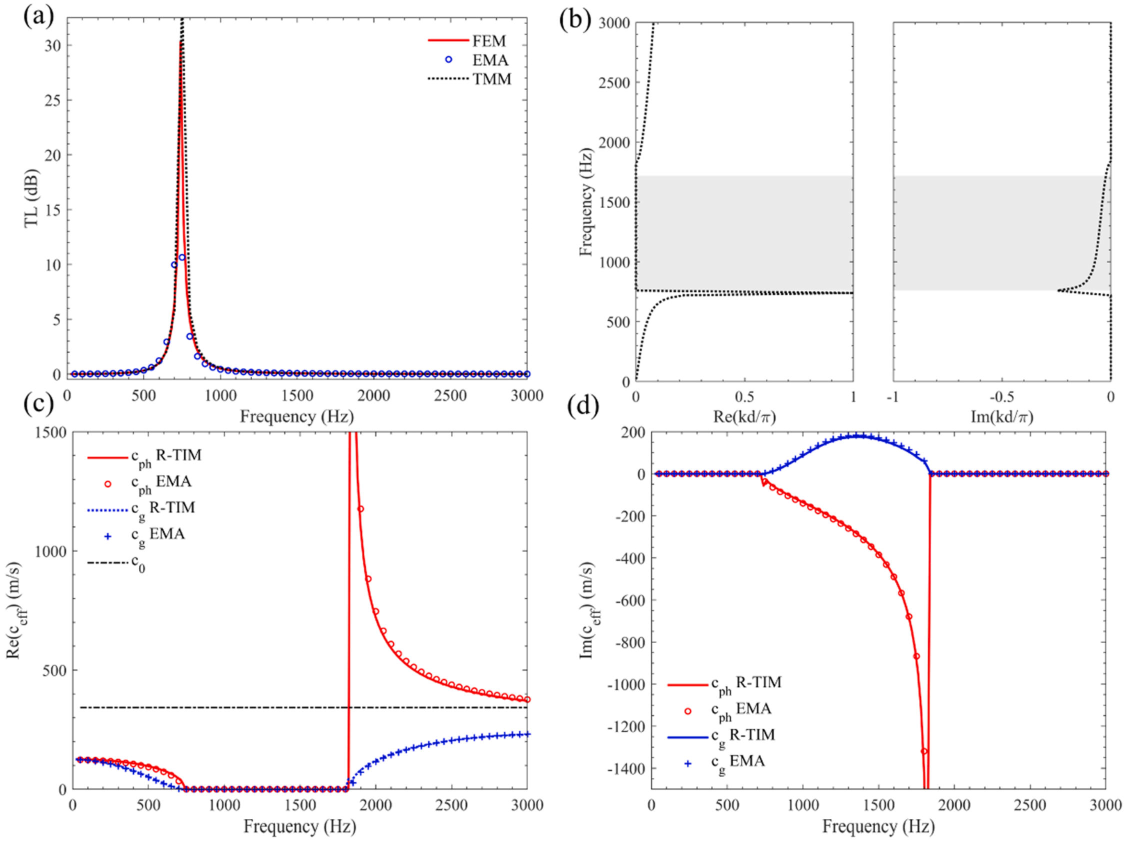

Fig. A5. (a) Transmission Loss (TL) calculated by FEM, EMA, and TMM. (b) Normalized dispersion relationship of the branched HR, calculated by R-TIM, real part (left), and imaginary part (right). (c) Real part and (d) imaginary part of the effective group and phase velocities.

Data availability

Data will be made available on request.

References

[1] J.-F. Allard, N. Atalla, Propagation of Sound in Porous media: Modelling Sound Absorbing Materials, 2nd ed., Wiley, Hoboken, N.J, 2009.
[2] L. Huang, A theoretical study of duct noise control by flexible panels, J. Acoust. Soc. Am. 106 (4) (1999) 1801–1809, https://doi.org/10.1121/1.427930.
[3] A. Mimani, M.L. Munjal, 3-D acoustic analysis of elliptical chamber mufflers having an end-inlet and a side-outlet: an impedance matrix approach, Wave Motion 49 (2) (2012) 271–295, https://doi.org/10.1016/j.wavemoti.2011.11.001.
[4] J.-P. Groby, R. Pommier, Y. Aurégan, Use of slow sound to design perfect and broadband passive sound absorbing materials, J. Acoust. Soc. Am. 139 (4) (2016) 1660–1671, https://doi.org/10.1121/1.4945101.
[5] N. Jiménez, V. Romero-García, V. Pagneux, J.-P. Groby, Rainbow-trapping absorbers: broadband, perfect and asymmetric sound absorption by subwavelength panels for transmission problems, Sci. Rep. 7 (1) (Dec. 2017) 13595, https://doi.org/10.1038/s41598-017-13706-4.
[6] J. Zhong, Z. Chai, J. Xiang, Double defects in trampoline effect and Helmholtz coupled acoustic metamaterial for broadband piezoelectric energy harvesting, Wave Motion 124 (2024) 103248, https://doi.org/10.1016/j.wavemoti.2023.103248.
[7] N. Fang, et al., Ultrasonic metamaterials with negative modulus, Nat. Mater. 5 (6) (2006), https://doi.org/10.1038/nmat1644. Art. no. 6.
[8] J. Mei, Z. Liu, W. Wen, P. Sheng, Effective mass density of fluid-solid composites, Phys. Rev. Lett. 96 (2) (2006) 024301, https://doi.org/10.1103/PhysRevLett.96.024301.
[9] R. Li, Q. Li, F. Gong, Z. Xiao, N. Qi, A latticed metamaterial with mutual conversion characteristics between pentamode and bandgap, Wave Motion 144 (2026) 103739, https://doi.org/10.1016/j.wavemoti.2026.103739.
[10] T.-Y. Huang, Y. Jing, Investigation of the effective density of arbitrarily shaped plate-type acoustic metamaterials without mass attached, Wave Motion 74 (2017) 124–133, https://doi.org/10.1016/j.wavemoti.2017.07.003.
[11] X. Yu, Y. Tong, J. Pan, L. Cheng, Sub-chamber optimization for silencer design, J. Sound Vib. 351 (2015) 57–67, https://doi.org/10.1016/j.jsv.2015.04.022.
[12] M. Malléjac, P. Sheng, V. Tournat, V. Romero-García, J.-P. Groby, Slow-sound-based delay-line acoustic metamaterial, Phys. Rev. Appl. 17 (4) (2022) 044035, https://doi.org/10.1103/PhysRevApplied.17.044035.
[13] M. Mironov, V. Pislyakov, One-dimensional acoustic waves in retarding structures with propagation velocity tending to zero, Acoust. Phys. 48 (2002), https://doi.org/10.1134/1.1478121.
[14] M. Červenka, M. Bednařík, Numerical study of the behavior of rectangular acoustic black holes for sound absorption in air, Wave Motion 123 (2023) 103230, https://doi.org/10.1016/j.wavemoti.2023.103230.

[15] S. Li, J. Xia, X. Yu, X. Zhang, L. Cheng, A sonic black hole structure with perforated boundary for slow wave generation, J. Sound Vib. 559 (2023) 117781, https://doi.org/10.1016/j.jsv.2023.117781.
[16] X. Zhang, L. Cheng, Broadband and low frequency sound absorption by Sonic black holes with Micro-perforated boundaries, J. Sound Vib. 512 (2021) 116401, https://doi.org/10.1016/j.jsv.2021.116401.
[17] J.-P. Groby, W. Huang, A. Lardeau, Y. Aurégan, The use of slow waves to design simple sound absorbing materials, J. Appl. Phys. 117 (2015), https://doi.org/10.1063/1.4915115.
[18] G. Theocharis, O. Richoux, V.R. García, A. Merkel, V. Tournat, Limits of slow sound propagation and transparency in lossy, locally resonant periodic structures, New J. Phys. 16 (9) (2014) 093017, https://doi.org/10.1088/1367-2630/16/9/093017.
[19] X. Zhu, et al., Implementation of dispersion-free slow acoustic wave propagation and phase engineering with helical-structured metamaterials, Nat. Commun. 7 (1) (2016) 11731, https://doi.org/10.1038/ncomms11731.
[20] E. Ballestero, N. Jiménez, J.-P. Groby, S. Dance, H. Aygun, V. Romero-García, Experimental validation of deep-subwavelength diffusion by acoustic metadiffusers, Appl. Phys. Lett. 115 (8) (2019) 081901, https://doi.org/10.1063/1.5114877.
[21] F. Ma, C. Liu, Y. Li, J.H. Wu, A thin-walled mesoscopic hybrid slit-resonator metamaterial absorber, Thin-Walled Struct 193 (2023) 111226, https://doi.org/10.1016/j.tws.2023.111226.
[22] J. Yang, J.S. Lee, Y.Y. Kim, Metaporous layer to overcome the thickness constraint for broadband sound absorption, J. Appl. Phys. 117 (17) (2015) 174903, https://doi.org/10.1063/1.4919844.
[23] J. Yang, J.S. Lee, Y.Y. Kim, Multiple slow waves in metaporous layers for broadband sound absorption, J. Phys. Appl. Phys. 50 (1) (2017), https://doi.org/10.1088/1361-6463/50/1/015301. Art. no. 1.
[24] J.-P. Groby, C. Lagarrigue, B. Brouard, O. Dazel, V. Tournat, B. Nennig, Enhancing the absorption properties of acoustic porous plates by periodically embedding Helmholtz resonators, J. Acoust. Soc. Am. 137 (1) (2015) 273–280, https://doi.org/10.1121/1.4904534.
[25] C. Lagarrigue, J.-P. Groby, V. TOURNAT, O. Dazel, O. Umnova, Absorption of sound by porous layers with embedded periodic arrays of resonant inclusions, J. Acoust. Soc. Am. 134 (2013), https://doi.org/10.1121/1.4824843.
[26] N. Jiménez, V. Romero-García, V. Pagneux, J.-P. Groby, Quasiperfect absorption by subwavelength acoustic panels in transmission using accumulation of resonances due to slow sound, Phys. Rev. B 95 (1) (2017) 014205, https://doi.org/10.1103/PhysRevB.95.014205.
[27] J. Li, L. Fok, X. Yin, G. Bartal, X. Zhang, Experimental demonstration of an acoustic magnifying hyperlens, Nat. Mater. 8 (12) (2009) 931–934, https://doi.org/10.1038/nmat2561.
[28] V. Fokin, M. Ambati, C. Sun, X. Zhang, Method for retrieving effective properties of locally resonant acoustic metamaterials, Phys. Rev. B 76 (14) (2007) 144302, https://doi.org/10.1103/PhysRevB.76.144302.
[29] X. Chen, T.M. Grzegorczyk, B.-I. Wu, J. Pacheco, J.A. Kong, Robust method to retrieve the constitutive effective parameters of metamaterials, Phys. Rev. E 70 (1) (2004) 016608, https://doi.org/10.1103/PhysRevE.70.016608.
[30] J. Pierre, V. Leroy, B. Dollet, A toy model for the effective density of acoustic metamaterials, Proc. R. Soc. Math. Phys. Eng. Sci. 478 (2261) (2022) 20210861, https://doi.org/10.1098/rspa.2021.0861.
[31] M.L. Munjal, 'The transfer matrix method', in Acoustics of Ducts and Mufflers with Application to Exhaust and Ventilation System Design, 1987. p. 75.
[32] V. Dubos, J. Kergomard, A. Khettabi, J.-P. Dalmont, D.H. Keefe, C.J. Nederveen, Theory of sound propagation in a duct with a branched tube using modal decomposition, Acta Acust. United Acust. 85 (1999) 153–169.
[33] X. Yu, Y. Mi, W. Zhai, L. Cheng, Principles of progressive slow-sound and critical coupling condition in broadband sonic black hole absorber, J. Acoust. Soc. Am. 154 (5) (2023) 2988–3003, https://doi.org/10.1121/10.0021880.
[34] L. Brillouin, Wave Propagation and Group Velocity, Academic Press, 2013.
[35] J. Kergomard, A. Garcia, Simple discontinuities in acoustic waveguides at low frequencies: critical analysis and formulae, J. Sound Vib. 114 (3) (1987) 465–479, https://doi.org/10.1016/S0022-460X(87)80017-2.
[36] G.H. Du, Z.M. Zhu, X.F. Gong, Acoustic Foundation, 3rd edn., Nanjing University Press, 2017.
[37] B.H. Song, J.S. Bolton, A transfer-matrix approach for estimating the characteristic impedance and wave numbers of limp and rigid porous materials, J. Acoust. Soc. Am. 107 (3) (2000) 1131–1152, https://doi.org/10.1121/1.428404.
[38] Committee. Test Method for Measurement of Normal Incidence Sound Transmission of Acoustical Materials Based on the Transfer Matrix Method, ASTM International, 2019. https://doi.org/10.1520/E2611-17.